3D-printed Soft Sensors for Adaptive Sensing with Online and Offline Tunable-stiffness

Liang He[1]*, Nicolas Herzig[2], Thrishantha Nanayakkara[3], and Perla Maiolino[1]

Abstract — The stiffness of a soft robot with structural cavities can be regulated by controlling the pressure of a fluid to render predictable changes in mechanical properties. When the soft robot interacts with the environment, the mediating fluid can also be considered an inherent information pathway for sensing. This approach to using structural tuning to improve the efficacy of a sensing task with specific states has not yet been well studied. A tunable stiffness soft sensor also renders task-relevant contact dynamics in soft robotic manipulation tasks. This paper proposes a type of adaptive soft sensor that can be directly 3D printed and controlled using pneumatic pressure. The tunability of such a sensor helps to adjust the sensing characteristics to better capturing specific tactile features, demonstrated by detecting texture with different frequencies. We present the design, modelling, Finite Element Simulation, and experimental characterisation of a single unit of such a tunable stiffness sensor. How the sensing characteristics are affected by adjusting its stiffness is studied in depth. In additional to the tunability, the results show such type of adaptive sensors exhibit good sensitivity (up to 2.6 [KPa/N]), high sensor repeatability (average std < 0.008 [KPa/N]), low hysteresis (< 6%), and good manufacturing repeatability (average std = 0.0662[KPa/N]).

1. INTRODUCTION

The information acquired via the tactile sensors allows the robot to estimate relevant states to perform delicate tasks, and to deal with uncertainties[1]. Research studies have been done extensively to replicate the sense of human touch in an artificial system[1,2] with approaches such as capacitive[3], piezoelectric[4], piezo-resistive[5], and optical[6] sensors. Recently, the growing attention to

---

[1] Liang He and Perla Maiolino are with the Oxford Robotics Institute, University of Oxford, OX2 6NN, UK
* email: liang.he@eng.ox.ac.uk
[2] Nicolas Herzig is with the Department of Engineering and Design, School of Engineering and Informatics, University of Sussex, BN1 9QT, UK
[3] Thrishantha Nanayakkara is with the Dyson School of Design Engineering, Imperial College London, SW7 2AZ, UK

unstructured soft interaction also raises the interest in developing soft tactile sensors that can undertake large-deformation[7].

Manufacturing sensors that are as soft as human tissue is challenging due to the limitation of the softness of the transducers[1]. High softness normally introduces high hysteresis and creep of the sensors[8]. To some degree, sensors based on computer vision can overcome such limitations[9]. However, those sensors are facing difficulties in complex contact modelling, limited sampling rate, constraint geometry, and size. Another critical factor limiting the application of soft tactile sensors is their adaptability and robustness when interacting with unstructured environments[10]. A tactile sensor can be very sensitive for a particular low-force range but easily saturate and damage when there is an unexpected high force[3].

Thus, this paper proposes a soft but stiffness-controllable sensor driven by pressurised air. The compressible media air allows the sensor to be extremely soft. Moreover, the sensor's stiffness, sensing range, and sensitivity are controlled by the driving pressure to match the specific task requirements.

Actuation and perception can be considered as an integration[10,11]. When an object interacts with the environment, the tactile measurements ultimately depend on the sensor configurations, especially in soft sensors. In other words, the physical property of the sensor/agent acts as a physical reservoir that filters the tactile information for active sensing. Such integration of perception and actuation is widely seen in nature. For instance, humans change finger stiffness and behaviour to maximize the gained tactile information for haptic explorations[12]. The active change of joint impedance helps humans maintain safe-interaction in high uncertainty tasks and high precision in a more constructed environment. The ability to vary the stiffness allows haptic information to be processed with various interaction modalities for state optimisation[13]. Analogy, the mice and rats also modulate their whisker movement to perform active sensing according to a specific environment by elaborately control the muscle of the follicle to bias the range of sensing from low to high frequencies[14]. Incorporating actuation in perception shows a new trend to develop robotic counterparts to understand the environment more effectively[11]. Another example can be found in active haptic exploration to localize a nodule in soft tissue with a tunable-stiffness robotic probe[15]. Examining the tissue with different stiffness of the probe can significantly reduce the uncertainty of the measured haptic information, thus, more effective in the detection.

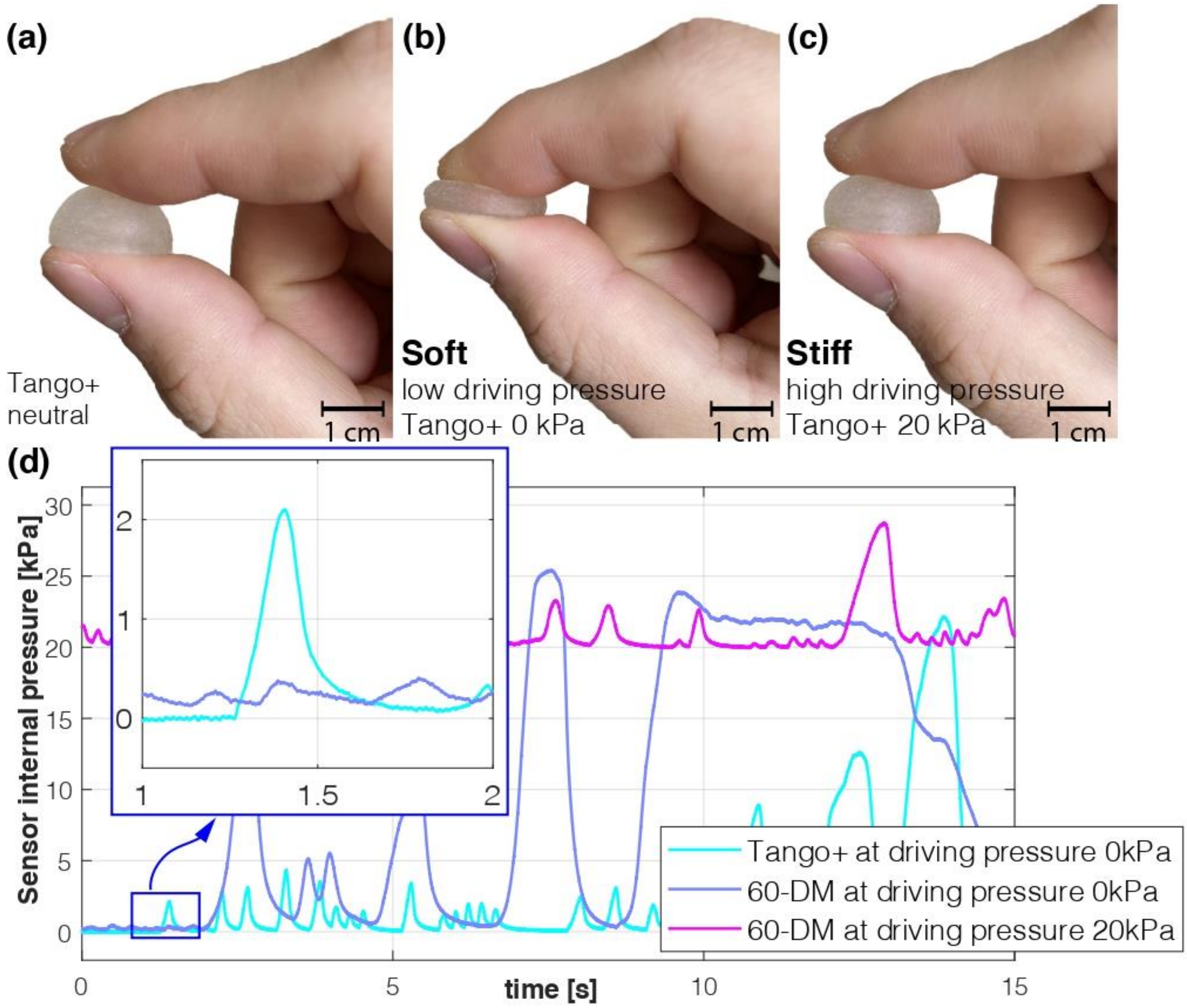

Fig. 1 (a) *A 3D printed soft sensor with Tango+ without contact and pressurisation.* **(b)** *A 3D printed soft sensor with Tango+ under compression with driving pressure of 0 kPa.* **(c)** *A 3D printed soft sensor with Tango+ under compression with driving pressure of 20 kPa.* **(d)** *Sensor response with external force applied for a 3D printed soft sensor with Tango+ under 0 kPa driving pressure, a 3D printed soft sensor with 60-DM under 0 kPa driving pressure, and a 3D printed soft sensor with 960-DM under 20 kPa driving pressure. A zoomed view of the detailed sensor response is shown. The sensor response was recorded at 10k Hz.*

While previous development of active sensing predominately relies on the stiffness and action change of the agent where the tactile sensor is mounted on a probe, coupled actuation and perception can also be incorporated in the sensor design itself[10]. This approach is particularly useful, considering that many robots interact with the environment directly with tactile sensors. The ability to change the characteristics of the soft sensor itself introduces three significant advantages. First, it can favour the sensing region actively. A similar example can be found in cameras that can change the focus. Secondly, it can enable sensing with different sensitivities without the need to use different sensors[16]. Tactile information can be unreliable when the contact is soft with large hysteresis. Sensing multiple iterations with different sensitivities would ultimately increase the confidence level. Thirdly, it can activate active sensing where the sensor can enable different interaction models by changing the contact stiffness. The mechanical property change can introduce a filtering effect of environmental noise and simplify further inference in information clustering[17].

The proposed adaptive soft tactile sensor (Fig. 1) presents tunable stiffness and controllable sensing characteristics for active sensing. The approach allows the sensors to be directly 3D printed with rubber-like materials and a further adjustment on the compliance with internal driving pressure. The online sensing characteristic change during the adjustment improve the efficacy of a sensing task with specific states. The tunability enabled a single sensor to interact with an object with different contact dynamics. The mechanical and associate sensing behaviour changes are characterised in this paper by theoretical modelling, finite element simulation, and experiments. We compared the performance and analysed the effect of material stiffness on sensing. Two-mode of sensor stiffness control can be achieved 1) offline-stage where the stiffness of the sensor can be changed via multi-material 3D printing; 2) online-stage where sensor physical properties are changed by tuning the internal fluid pressure. A texture detection experiment is included to show the advantage of having a tunable sensor, with results indicating that a single sensor can be favoured in detecting various textures by control its stiffness. In general, results show that this methodology developed tunable-stiffness sensors with good sensitivity (up to 2.6 [KPa/N]), high sensor repeatability (average std < 0.008 [KPa/N]), low hysteresis (< 6%), and good manufacturing repeatability (average std = 0.0662[KPa/N] of 6 groups of 18 samples).

2. DESIGN AND MODELLING

A. Basic structure and working mechanism of the tunable stiffness soft sensor

When a soft sensor actively interacts with a solid object, both agents are subjected to external forces with deformation associated with internal stresses and strains. Unlike soft sensors with fixed features, where the material properties are only characterised as the parameter to determine absolute sensor responses[18], the proposed tunable stiffness sensor determines the sensing model based on the physical property. This active sensing framework is demonstrated by exploring the inherited sensing characteristics with pressurised fluid[19], where significant sensing characteristics and stiffness change is exhibited during inflation.

The proposed sensor incorporates a 3D printed soft membrane to form a closed cavity that can be pressurised via an air source (Fig. 1). Rubber-like materials with the Polyjet 3D-printing technique introduced controllable membrane stiffness in the design phase (Object-260). Deformation of the soft architecture is triggered when an external force is applied to the soft membrane. According to Boyle's law, such changes in the cavity volume will be reflected via the pressure variation. Thus, the pressure variation reflects the exerted force between the tactile sensors and the environment. In addition, the sensor's mechanical properties and sensing characteristics are controlled by the internal pressure. The sensor exhibits different interaction models to the environment depending on whether it is soft (low driving pressure) or stiff (high driving pressure). Two parameters for regulating the sensor stiffness are defined as 1) the offline parameter membrane stiffness (Tango+ and Digital materials-DM, see Table.1 and Supplementary-A) and 2) the online parameter internal driving pressure.

B. Theoretical modelling

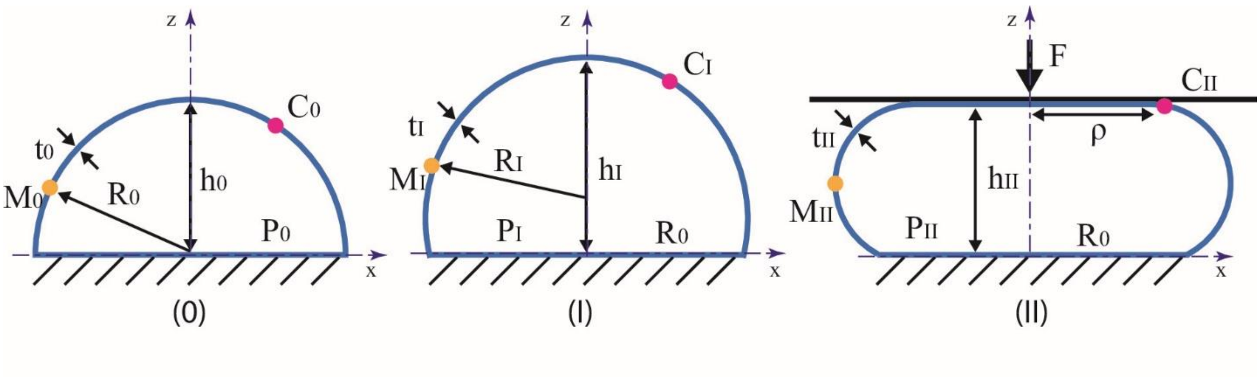

Fig. 2 *Theoretical modelling of the sensor. State 0 is the neutral state of the sensor with internal driving pressure equal to atmospheric pressure. State I is the pressurised state where the internal driving pressure is subjected to a positive pressure higher than the atmospheric pressure. State II is the state where the sensor is subjected to external load when interacting with a solid body. The material points of the membrane are defined with points* M_0, M_I, *and* M_{II} *for the three states, respectively. The extent of contact during the interaction is characterised by the radius of the contact* ρ, *shown with material point* C_{II} *at the edge of contact in the deformed membrane.*

The sensor is modelled under the assumption of a hyperelastic membrane via three different states depending on its driving pressure and contact status. h is the distance to the membrane from the origin. When the driving pressure P is equal to P_0 (atmospheric pressure), the sensor is considered as a hemispherical membrane with an uninflated radius R_0 ($h_0 = R_0$) and initial thickness t_o(state 0, Fig. 2). Considering the sensor is driving by a positive internal pressure P_I ($P_I > P_0$), state I is inflated to a spherical cap with the height of h_I and base radius of R_0, Fig. 2-I. State II is considered when a rigid surface is coming in contact and pressing the sensor symmetrically (Fig. 2-II). Constant curvature of the non-contact part of the sensor membrane is considered with an assumption of the curvature tangential to the contact surface during the deformation. The membrane of the sensor is modelled as homogeneous, isotropic, and incompressible material[20].

The principal stretch ratios for the membrane are defined as $\lambda_\phi,\ \lambda_\psi,$ and λ_t, where λ_ϕ and λ_ψ are for the lateral directions and λ_t is the stretch ratio normal to the membrane.

The right Cauchy–Green deformation tensor 1st and 3rd principal invariant with incompressibility condition[20] are given by:

$$I_1^C = \lambda_t^2 + \lambda_\phi^2 + \lambda_\psi^2 \tag{1}$$

Assuming the silicone membrane material is incompressible with equibiaxial deformation $\lambda_\phi = \lambda_\psi$, the principal stretch ratios are determined by:

$$\lambda_t \lambda_\phi \lambda_\psi = 1 \tag{2}$$

$$\lambda_t = \frac{1}{\lambda_\phi^2} = \frac{1}{\lambda_\psi^2} = \frac{t_1}{t_0} = \lambda_I \tag{3}$$

Where λ_I denotes the normal stretch ratio from state 0 to state I. The volume of the fluid V_g within the sensor cavity is obtained:

$$V_g = \frac{1}{6}\pi h_I ({3R_0}^2 + {h_I}^2) \tag{4}$$

Considering constant volume of the membrane $V_m = V_{mI} = V_{m0} = 2\pi {R_0}^2 t_0 = \pi\left({R_0}^2 + {h_I}^2\right)t_I$

$$\lambda_I = \frac{2{R_0}^2}{\left({R_0}^2 + {h_I}^2\right)} \tag{5}$$

The total potential energy E_p can be expressed as:

$$E_p = \int p\, dV_g + \int w\, dV_m \tag{6}$$

Taking the assumption of neo-Hookean material, the strain energy density function:

$$w = C_1(\lambda_I^2 + 2\lambda_I^{-1} - 3) \tag{7}$$

Thus,

$$E_p = -p\frac{1}{6}\pi h_I\left(3{R_0}^2 + {h_I}^2\right) + 2\pi {R_0}^2 t_0 C_1(\lambda_I^2 + 2\lambda_I^{-1} - 3) \tag{8}$$

Applying the principle of steady state minimum total potential energy, assuming h_I and p are only system variables, h_I can be solved with $\frac{\delta E_p}{\delta h_I} = 0$. The driving pressure p can be expressed by $p_I =$

$k(h_I)$. Considering the nonlinear function k also depends on the types of hyperplastic material model being used to obtain the strain energy function, neo-Hookean material model is represented with reduced system order to visualize the relation of the sensor geometry to the driving pressure and material stiffness.

$$p_I = k(h_I, C_1) \tag{9}$$

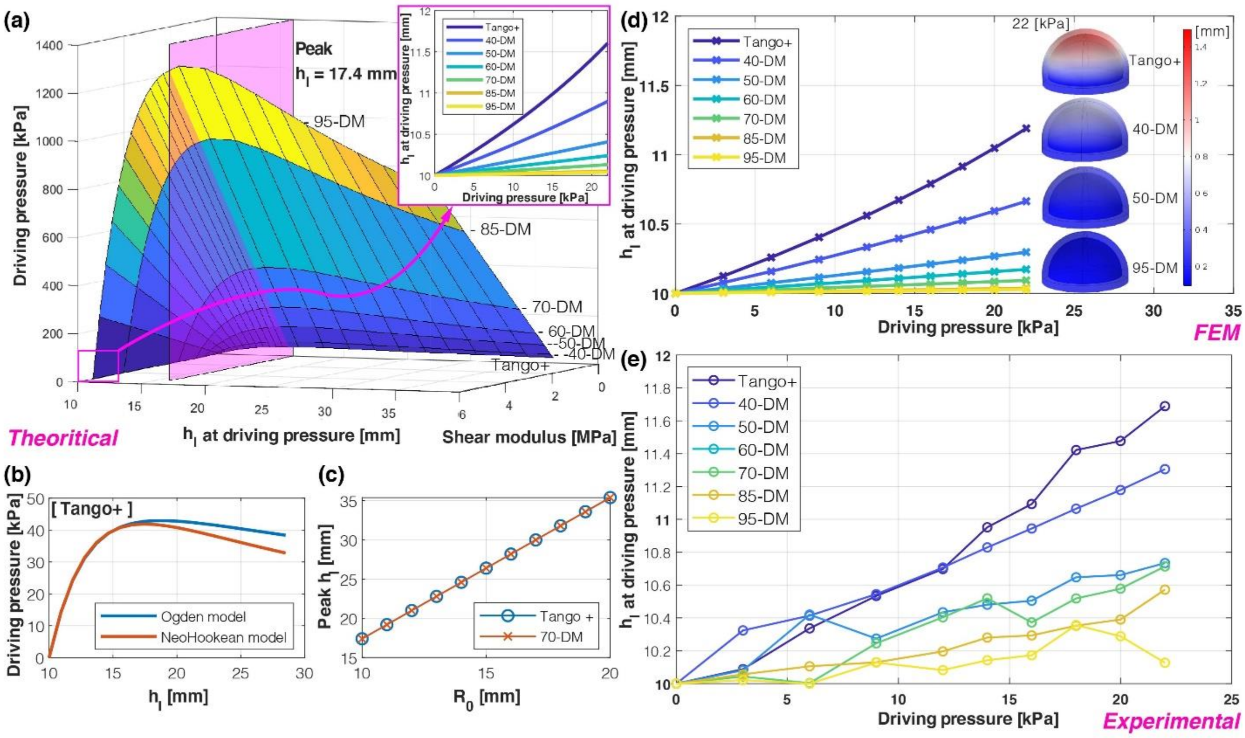

Fig. 3 *Theoretical model, FEM simulation, and experimental characterisation of the soft sensors from state 0 to state I.* ***(a)*** *theoretical modelling of the sensor under continuous inflation with Tango+ and all DM materials. Neo-Hookean model with shear modulus used in Table. 1 indicates the material stiffness. A clear "snap buckling" behaviour can be observed during the inflation with the peaks always exhibits when* $h_I =$ 17.4 *mm regardless of the membrane stiffness. The "snap buckling" presents with the maximum driving pressure, as it increases with the increase of membrane stiffness. The lowest maximum driving pressure with the sensor made from Tango+ is around 42 kPa. A zoom view of the sensor geometry change (theoretical) is also presented between driving pressure 0 to 22 kPa.* ***(b)*** *Comparing the Ogden hyperplastic material model of Tango+ obtained from* [25] *with the neo-Hookean material model.* ***(c)*** *The theoretical model indicates that the peak* h_I *at the "snap buckling" point exhibits a linear relation to the size of the sensor. However, the peak* h_I *is independent of the material stiffness.* ***(d)*** *The geometry changes of the soft sensors with*

increased driving pressure, results from FEM. The deformation of the sensors made from Tango+, 40-DM, 50-DM, and 95-DM at the driving pressure of 22 kPa is shown. The colour bar indicates the deformation in [mm]. ***(e)*** *The geometry changes of the soft sensors with increased driving pressure, results from experimental characterisations.*

Fig. 3(a) shows the theoretical simulation of the sensor during continuous inflation from state 0 to sate I. The sensor exhibits a clear maximum driving pressure during the inflation due to the material hyperelasticity[21]. This 'snap buckling' behaviour is commonly observed in many rubber-like materials where a punctuated reduction of pressure can be observed once it reaches the peak internal pressure [21,22]. The 'snap buckling' effect happens when the sensor height h_I approaches 17.4 mm based on the given sensor geometry ($R_0 = 9.25\,mm, t_0 = 1.5\,mm$). This peak h_I at the maximum driving pressure value is only affected by the original sensor diameter in regardless of the membrane stiffness. However, softer material used for the sensor is subjected to larger volume change under the same driving pressure. A linear relation between sensor diameter R_0 and peak h_I can be observed while the result shows no difference between Tango+ and 70-DM (Fig. 3(c)). Ogden model (parameters from[25]) was also used to do a comparison to the neo-Hookean model, with neglected difference exhibits before the sensor reaches the peak h_I (Fig. 3(b)). For the ease of sensor characterisation and modelling, the sensor is only evaluated before it reaches the maximum driving pressure (peak h_I).

State I to state II is modelled by assuming an object with an infinite area exerting an applied force F and a displacement $\Delta\delta = h_I - h_{II}$. The deformation of the membrane is modelled as an asymmetric discotic spherocylinder, Fig. 2(c).

Assuming 2D axisymmetric revolution and the axis origin at the base centre of the sensor, the volume of cavity is:

$$V_{gt} = \int_0^{h_{II}} \pi[\xi(z)]^2\,dz \tag{10}$$

Where z represents the distance to the material point of the sensor membrane in the z coordinate and the function $\xi(z)$ represents the x coordinate of the material point given by

$$\xi(z) = \sqrt{\left(\frac{{h_{II}}^2 - (R_0 - \rho)^2}{2h_{II}}\right)^2 + (R_0 - \rho)^2 - \left(z - \frac{{h_{II}}^2 - (R_0 - \rho)^2}{2h_{II}}\right)^2} + \rho \qquad (11)$$

Considering constant material volume of the membrane with the assumption of incompressibility:

$$\pi\left({R_0}^2 + {h_I}^2\right)t_I = \pi\rho^2 t_{II} + 2\pi\int_0^{h_{II}} \xi(z)\sqrt{1 + [\xi'(z)]^2}\, dz\, t_{II} \qquad (12)$$

Thus,

$$\lambda_{II} = \frac{t_{II}}{t_I} = \frac{\pi\left({R_0}^2 + {h_I}^2\right)}{\pi\rho^2 + 2\pi\int_0^{h_{II}} \xi(z)\sqrt{1 + [\xi'(z)]^2} dz} \qquad (13)$$

Again, consider the minimum total potential energy principle and the neo-Hookean model:

$$E'_p = -p_{II}V_{gt} + 2\pi {R_0}^2 t_0 C_1(\lambda_{II}^2 + 2\lambda_{II}^{-1} - 3) - F\Delta\delta \qquad (14)$$

Assume Boyle's law pv is constant,

$$(p_{II} + p_m)V_{gt} = (p_I + p_m)V_g \qquad (15)$$

the applied force is determined by:

$$F = p_{II}\, \pi\rho^2 \qquad (16)$$

then

$$E'_p = -p_I V_g + 2\pi {R_0}^2 t_0 C_1(\lambda_{II}^2 + 2\lambda_{II}^{-1} - 3) - \left(\frac{(p_I + p_m)V_g}{V_{gt}} - p_m\right)\pi\rho^2(h_I - h_{II}) \qquad (17)$$

Substituting (10) and (13) into (17), assuming $\frac{\delta E'_p}{\delta h_{II}} = 0$ under the boundary condition $0 < \rho < R$.

The increase of pressure and force can be obtained with the following nonlinear equations:

$$\Delta p = f(p_I, \Delta\delta) \qquad (18)$$

And,

$$F = \varphi(p_I, \Delta\delta) \qquad (19)$$

C. *Finite element modelling (FEM)*

FEM with COMSOL 5.3a are employed in the study to simulate the soft sensor physical behaviour under positive pressure and estimate the change of sensing characteristics reflected by internal pressure variations. In contrast to the membrane model used in the theoretical simulation, the FEM is determined with a solid mechanics model to reveal the contribution of structural stiffness. The FEM simulation is performed in two studies: (1) the sensor is pressurised freely with a defined driving pressure from state 0 to state I, (2) a rigid indenter is introduced in state II to exert regulated loading with step control. In study 2, the internal pressure is solved based on the result of study 1 and the governing sensor deformation. See Supplementary-B for details of the simulation setup.

Table. 1 Material properties

Material Type	**Tango +**	**40-DM**	**50-DM**	**60-DM**	**70-DM**	**85-DM**	**95-DM**
Shore A (STD)	27.6 (1.0)	38.5 (1.5)	50.4 (1.6)	59.9 (2.0)	68.9 (1.4)	80.4 (1.6)	91.3 (2.1)
Shore A -after one year (STD)	29.5 (1.8)	42.4 (1.8)	51.1 (1.8)	60.5 (1.5)	68.2 (1.2)	76.0 (1.5)	87.0 (1.8)
p-value	<0.01	<0.01	0.2112	0.2648	0.0556	<0.01	<0.01
Shore A change	-6.61 %	-9.2 %	-1.37 %	-1.03 %	0.99 %	5.8 %	4.98 %
Shear modulus (MPa)	0.17	0.27	0.55	0.91	1.64	4.00	5.33

The p-value is calculated with one-sample and paired-sample t-test for the measured shore A hardness before and after one year, testing the null hypothesis that the pairwise difference between the two measurements has a mean equal to zero. In this study, the density of all the materials is modelled as 1.15 g/cm3 with the Poisson's ratio of 0.49.

3. EXPERIMENTAL CHARACTERISATION

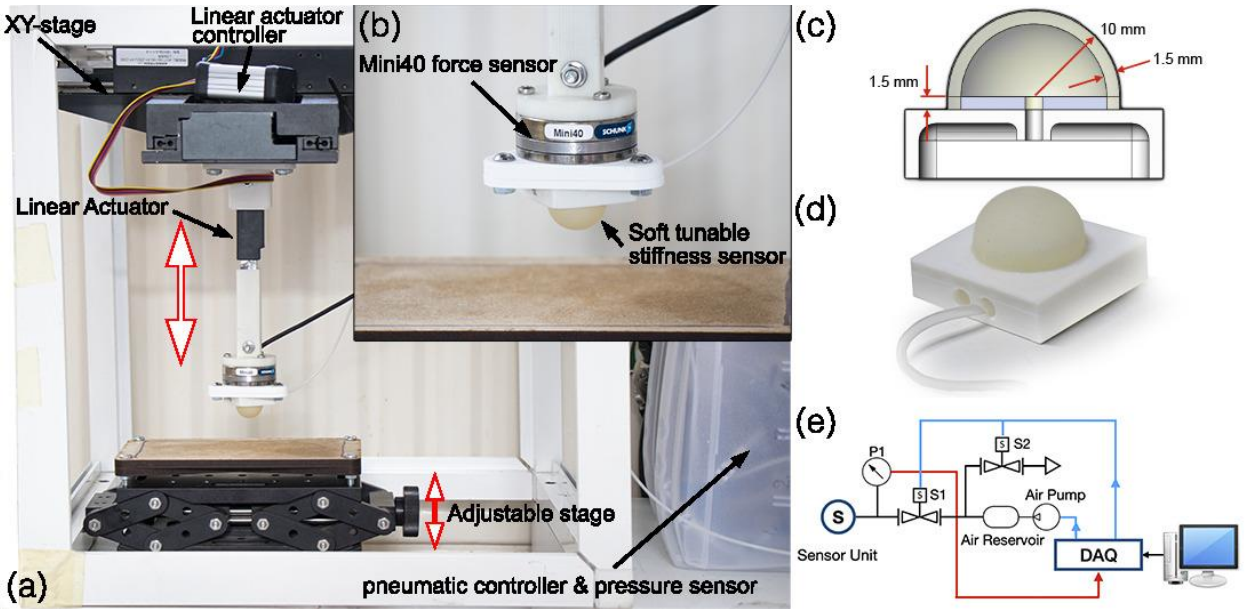

Fig. 4 *Setup for the sensor characterisation.* ***(a)*** *The indentation setup with a cartesian robot.* ***(b)*** *A closer view of the soft sensor mounted on the indenter.* ***(c)*** *Schematics and dimensions of the soft sensor.* ***(d)*** *The 3D printed soft sensor is mounted on a rigid connector (ABS, 3D printed) for testing.* ***(e)*** *The pneumatic connection diagram to control the sensor driving pressure and record the internal pressure variation.*

A. Characterisation Setup

The sensor experimental characterisation was conducted with a 3-axis Cartesian robot, performing indentation tests against a flat surface with the sensor mounted on the indenter (Fig. 4). Details about the setup and data acquisition can be found in Supplementary-C.

B. Sensitivity and Repeatability

To evaluate the sensitivity and repeatability of the sensor, the characterisation is conducted with robot position control. The probe moved along the z-axis to a specified z-position and stayed at the position for 4 seconds, and it returned to the initial no-contact position. A step-increment (0.5 mm step) indentation was repeated until the sensor reached the defined maximum deformation (three-quarters of the original sensor radius R_0 to avoid damage). We repeated this test three times for seven soft tactile sensors (Tango+, 40-95 DM) at each driving pressure (~450 indentations for each sensor). Between each indentation, we waited 30 seconds and reset the pressure value to remove any hysteresis effect. The sensitivity S of the sensors are defined as $\Delta P/\Delta F$, where ΔP is the internal pressure variation and ΔF denotes the applied force.

C. *Saturation, Sensing Range, and Hysteresis*

Previous tests set the maximum deformation as three-quarters of the sensor radius. In this part, we tested the soft sensor until it saturates. The sensing range and hysteresis are also evaluated with this test. All sensors (Tango+, 40-95 DM) were tested with a comparison between driving pressure $0\ kPa$ (soft state) and $12\ kPa$ (stiff state). The tests were performed with the same load-unload pressure cycle, as mentioned previously. However, the waiting time between each indentation was reduced to 2 seconds, and the internal pressure was not reset.

4. RESULTS AND DISCUSSION

In the following section, we compared the results from the theoretical study (solved numerically with Matlab 2020a), FEM simulation, and empirical characterisation. The sensor stress relaxation, manufacturing repeatability, and the effect of aging are also experimental tested (Supplementary-D and E)

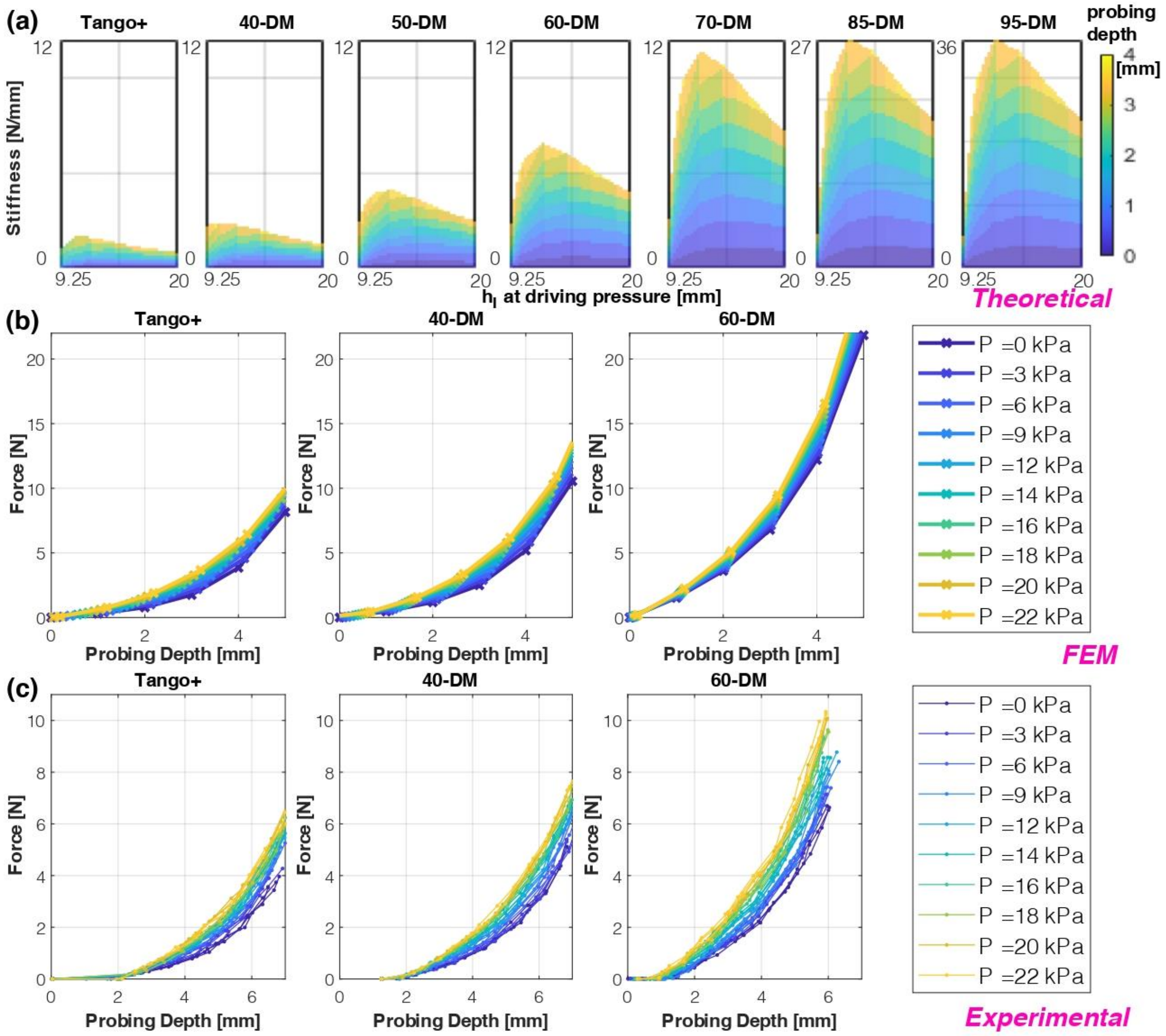

Fig. 5 *Selected results of sensor mechanical property change with both online (driving pressure) and offline (membrane stiffness) parameters.* ***(a)*** *The theoretical modelling result. The colour bar indicates the probing depth of the indentation. The x-axis is the geometry data of the sensor with* h_I *(state I) at a specific driving pressure. The y-axis is the sensor stiffness characterised by* $dF/d\Delta h$. ***(b)*** *The result from FEM studies. Indentation force with probing depth for sensors with increased driving pressure.* ***(c)*** *The result from experimental characterisation. Indentation force with probing depth for sensors with increased driving pressure. All three-trial data on three identical sensors for each driving pressure are shown in the subplot*

for Tango+, 40-DM, and 60-DM. Good repeatability of all sensors can be observed. The full set results for all materials can be found in Supplementary ***Fig. S3.***

A. *Tunable stiffness*

The sensor stiffness is the contribution of structural stiffness and pressurisation of the sensor cavity. The theoretical model focused mainly on the effect of pressurisation with a membrane assumption while the FEM simulation represents both contributions. Results of theoretical model, FEM, and experimental characterisation are reported in Fig. 5 (a), (b), and (c), respectively. A clear increase of the stiffness can be observed with the increase of indentation depth denoting the non-linear mechanical property. The stiffness (shown in Fig. 5 (a)) is defined as $dF/d\Delta h$, where F is the applied load on the soft sensor and Δh is the indentation depth. Results from the theoretical model indicate that the increase of driving pressure would increase the sensor stiffness before the driving pressure reaches the maximum driving pressure where $h_I\ = 17.4\,mm$. With further inflation, the sensor stiffness drops after the maximum driving pressure is reached, representing the membrane 'snap buckling'.

Thus, we define the pressure region lower than maximum driving pressure as the valid pressure-based control region for tunable stiffness. FEM and experimental results also validate the feasibility of controlling sensor stiffness with internal driving pressure. However, it needs to be noted that when the material stiffness is increased, the required change on driving pressure to increase the internal driving pressure is also increased significantly due to the increased structural stiffness.

B. *Sensitivity and Repeatability*

The sensitivity S of the sensors are defined as $\Delta P/\Delta F$, where ΔP is the internal pressure variation and ΔF denotes the applied force. The result of FEM simulation shows the change of the internal pressure and applied force at each indentation depth, Fig. 6 (a). Selected detailed result with a clear linear relation of the sensitivity is shown in Fig. 6 (d)-(f). The estimated sensitivity with a linear model in Fig. 6 (g). Sensors made from soft material Tango+, 40-DM, 50-DM, 60-DM show a decrease in sensitivity with the increase of driving pressure, while sensors made from stiff material exhibit a slight increase in sensitivity with increased driving pressure. Sensor made from 70-DM shows neglected change in sensitivity up to the driving pressure of 22 kPa. Full results see Supplementary-F.

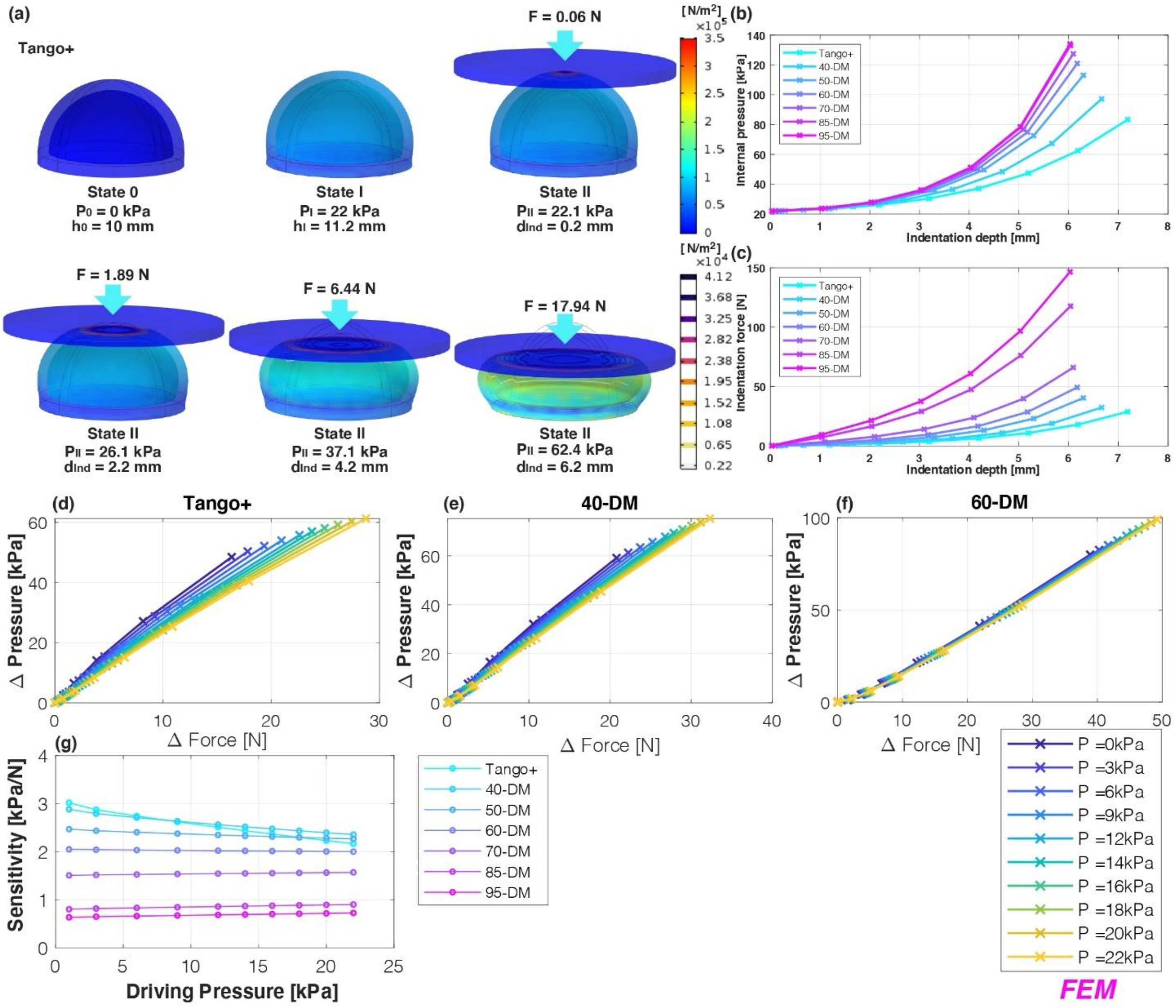

Fig. 6 *Selected sensitivity results from the FEM study.* ***(a)*** *Result of the sensor made from Tango+ under 22 kPa driving pressure, from state 0, I, to II. The deformation, the von Mises stress on the surface, and the contact pressure are shown.* ***(b)*** *and* ***(c)*** *Internal pressure and force data for all sensors made from different materials at the driving pressure of 22 kPa.* ***(d)-(f)*** *The results of sensor response ΔP at different applied forces ΔF is shown in (d) to (f) for membrane materials of Tango+, 40-DM and 60-DM, respectively.* ***(g)*** *The overall sensitivity changes of the soft sensors made from different materials with increased driving pressure. The full set results for all materials can be found in Supplementary* ***Fig. S4.***

The theoretical result (Fig. 7(a)) shows decreases in the sensitivity for the soft sensors with increased driving pressure. However, minimum sensitivity region can be observed in the model. This minimum region is assumed to happen when the driving pressure is approaching the maximum pressure, while a slight increase of sensitivity exhibits after the snap-through. The model also indicates high linearity of the sensor response between ΔP and ΔF, with R squared values reported in Fig. 7(b).

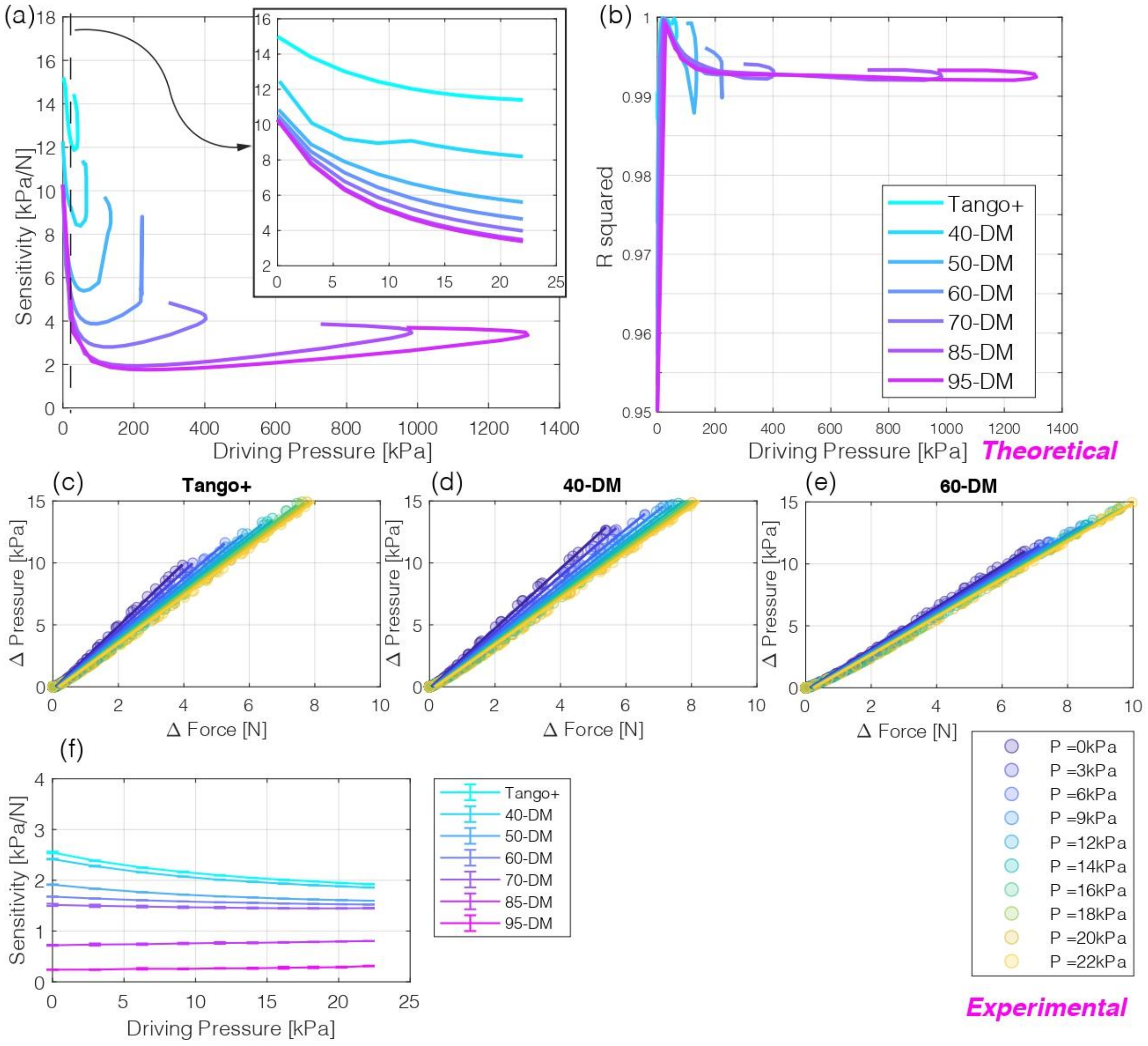

Fig. 7 ***(a)*** *Theoretical result of the sensor sensitivity change with increased driving pressure. A zoom view of the experimental tested low-pressure (<22 kPa) region is shown. Part of the curve show two sensitivity values due to the existence of material "snap bulking." During inflation, the membrane will continue to increase its volume after the maximum pressure is reached, yet with reduced internal pressure.* ***(b)*** *Linearity*

of the sensor response with ΔP and ΔF is represented with R squared value at each driving pressure. ***(c)-(e)*** *Selected experimental sensor response with the three trials of repetition on identical sensor samples for sensor made from Tango+, 40-DM, and 60-DM. A linear model is used to fit the sensor response.* ***(f)*** *The overall sensitivity changes of the soft sensors made from different materials with increased driving pressure. Standard deviation error shown for repeated tests on three identical samples. Average STD for Tango+, and 40-95 DM are 0.0051, 0.0035, 0.0022, 0.0035, 0.0138, 0.0109, 0.0108, respectively. The average STD for all sensors is 0.0071. The full set results for all materials can be found in Supplementary* ***Fig. S5.***

The experimentally characterised sensor responses under different driving pressures are reported in Fig. 7(c)-(e) for sensors fabricated with Tango+, 40-DM, and 60-DM, respectively.

The highest sensitivity case S= 2.6 [KPa/N] happens at the softest tactile sensor fabricated by tango+ under the lowest driving condition. By increasing the material stiffness, the sensitivity also drops monotonically, which the trend is aligned with the FE simulation result and mathematical model

Overall, for tactile sensors that were fabricated by a softer material (Tango+, 40-DM), the sensitivity drops when the internal driving pressure increase. However, for tactile sensors fabricated by stiffer material such as 85-DM and 95-DM, the sensitivity increases with the increase of internal driving pressure. This is due to the fact the material is so stiff that the increase of sensor stiffness caused by an increase of internal pressure is too small compared to the material stiffness. Thus, the increase of stiffness can be neglected unless the sensor is pressurised to a much higher region. Without the contribution of material stiffness, the sensor is more sensitive at higher pressurised conditions. By contrast, the drop of sensitivity at higher pressurised conditions for soft sensors caused by the increase of sensor stiffness (less strain deformation for the same amount of stress) compensates this increase of sensitivity caused by an increase of internal driving pressure. The two phenomena fully compensate each other for sensor fabricates by 70-DM, where a flat line of sensitivity can be observed in Fig. 7(f) for the specific sensor. This behaviour is in alignment with the FEM simulation in Fig. 6(g). Fig. 7(j) also included the standard deviation of the sensitivity in three trials of characterisation, where excellent repeatability can be observed (average std < 0.008).

C. *Saturation, Sensing Range, and Hysteresis*

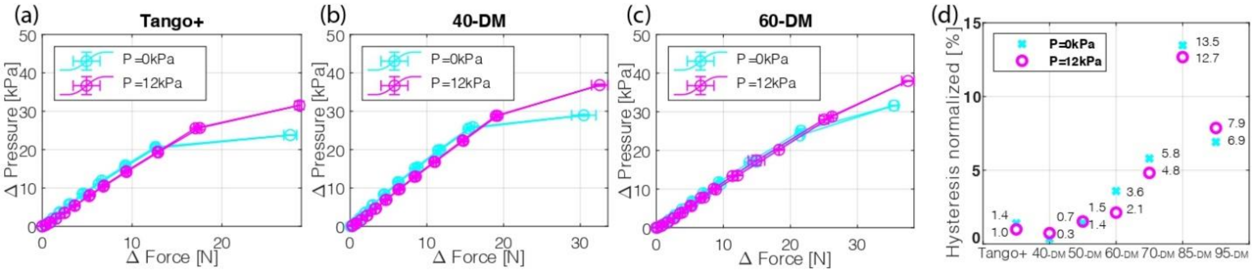

Fig. 8 *Selected result of continuous loading tests. The result of sensors made from Tango+, 40-DM, and 60-DM are shown in* ***(a)*** *to* ***(c)****, respectively. All sensors are tested in three trials with the driving pressure of 0 kPa and 12 kPa. Sensors are tested upon saturation during the test.* ***(d)*** *Normalised hysteresis. The full set results for all materials can be found in Supplementary* ***Fig. S6.***

The experimental results in Fig. 8 show the sensor response under repeated loading conditions upon saturation with two selected driving pressures (0 and 12 kPa). The sensing range increased with the increase of driving pressure. This effectively solved the issue that many soft sensors are only sensitive at a low-force region while getting easily saturated when the force increases. In addition, the sensors made from Tango+, 40-DM, 50-DM, 60-DM, and 70-DM exhibit neglected hysteresis ($< 6\%$). The hysteresis is considerably low compared to many piezoresistive[26], capacitive[3] sensors and sensors made of conductive rubber[27] reported from literature[1]. Together with the high-frequency sampling rate (10kHz), the sensor shows good potential in dynamic interaction. Indeed, the sensor hysteresis increases with the increase of material stiffness. The hysteresis for the stiff sensors made from 85-DM and 95-DM is still considerably low ($< 14\%$) compared to conductive polymer-based soft sensors. Full results see Supplementary-F.

5. ONLINE TUNABLE STIFFNESS IN SOFT TEXTURE DETECTION

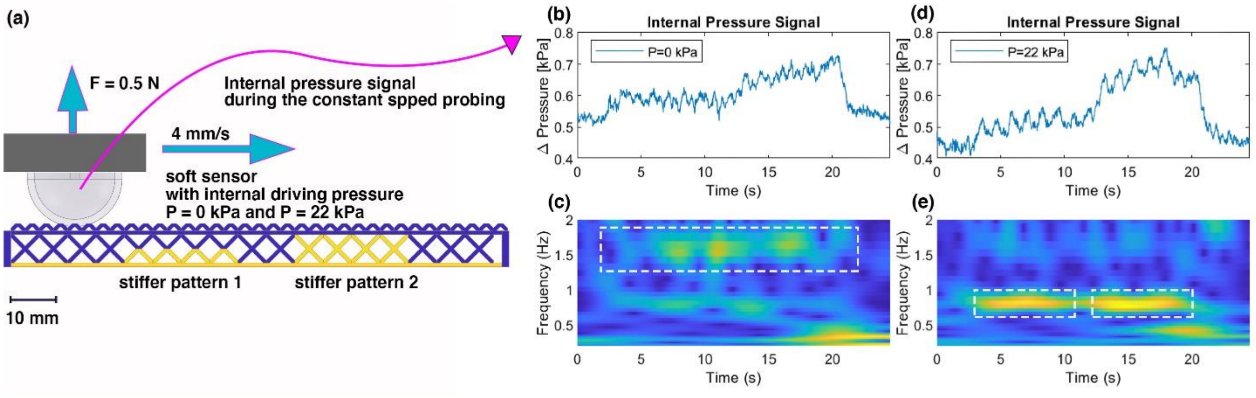

Fig. 9 (a) The online tunable stiffness of the sensor is tested by detecting the texture of a multilayer lattice structure. The sensor (fabricated with Tango+) is being inflated to two states during the tactile exploration. The driving pressure P= 0 kPa for the soft state. The driving pressure P=22 kPa for the stiff state. The sensor is first applied to the structure with the normal force of 0.5 N for both states, then moved with a constant speed of 4 mm/s to detect the texture in the multilayer lattice structure. PTFE lubricant is applied to the sensor surface to reduce friction. The multilayer lattice structure (3D printed with J735, Stratasys Ltd., USA) is made of two materials. The blue-region material (Agilus30 is a soft and rubber-like material with a quoted tensile strength of 2.1-2.6MPa and Shore hardness of 30A, Stratasys Ltd.) and the yellow-region material (Vero is a rigid plastic-like material with a quoted tensile strength of 50-65MPa and a Shore hardness of 83-86D). The distance of the higher-frequency surface pattern is around 3 mm. The distance of the lower-frequency buried pattern is around 6 mm. Considering the probing speed of 4 mm/s, the computed baseline frequency for the lower-frequency pattern is around 0.75 Hz, and the computed baseline frequency for the lower-frequency pattern is around 1.5 Hz. **(b)** The internal pressure signal during the detection at its soft state with 0 kPa driving pressure (signal recorded at 10k Hz). **(d)** The internal pressure signal during the detection at its stiff state with 22 kPa driving pressure (signal recorded at 10k Hz). **(c)** The result of the continuous wavelet transform of the soft state sensor signal. A sharper detection of the higher-frequency surface structure is found around 1.5 Hz. **(e)** The result of the continuous wavelet transform of the stiff state sensor signal (analytic Morse wavelet). A sharper detection of the lower-frequency buried structure is found around 0.75 Hz. Both stiffer patterns 1 and 2 are detected with a sharper detection of pattern 2.

To demonstrate the advantage of tuning the sensor stiffness during tactile exploration, a soft sensor (Tango+) is used to detect the texture of a multilayer lattice structure. The experiment is performed with the same setup introduced in Supplementary-C. Fig. 9a shows the experimental protocol with the multilayer lattice structure being examined. The sensor is first inflated to its defined driving pressure (0 kPa as the soft state and 22 kPa as the stiff state) and then perform an indentation with the normal force equal to 0.5 N. The texture is then detected by probing the lattice structure with the sensor at a constant speed of 4 mm/s. The internal pressure signal during the probing is shown in Fig. 9 b and d. By analysing the sensor response in the frequency domain with a continuous wavelet transform, the result shows a significant change for the same sensor at its soft and stiff state (Fig. 9 c and e). Although the applied force is the same for both states, the sensor at soft state shows a sharper distribution in detecting the higher-frequency surface texture while the sensor at stiff state shows a better performance in detecting the lower-frequency texture. Fig. 9 e shows a clear distribution of both regions of buried texture with a sharper detection of the stiffer pattern 2 since it is closer to the surface. This experiment demonstrates the use of online sensor stiffness tuning in better detecting various features compared to sensors with only fixed characteristics.

6. CONCLUSIONS

In this paper, we show that tunable stiffness soft sensors help to estimate task-relevant states while filtering others. Pneumatic-based soft sensing with elastomeric materials is promising due to the low cost of pressure sensors, compact size, and ease of integration in soft robotic systems. Controlling the mediating fluid of such a sensor allows it to favour its sensing characteristics to adapt to the environment as an online parameter. If a soft sensor is only implemented with a fixed sensitivity and mechanical property, multiple sensors with different sensing characteristics are commonly needed to detect different features. For instance, Interlink's commercial tactile sensors are developed with different sensing ranges (0.2 to 20 N, 0.3 N to 50 N, and 0.5 N to 150 N).

Creating tunable contact dynamics in specific tasks also requires the assembly of filters to a fix-property sensor.

Indeed, the proposed sensor can be designed in many shapes and dimensions. We choose to test the sensor by fabricating it in the hemispherical shape for the purposed of ease on generalisation, modelling, and characterisation. A theoretical model with membrane assumption, FEM with neo-Hookean solid mechanics simulation, and experimental characterisation all validate the feasibility to tune the sensor mechanical property and sensing characteristics with the combination of online and offline parameters.

This study opens up new opportunities to integrate 3D printed soft sensors for active perception. In contrast to passively relying on the static tactile information from sensors that have large variability during soft interaction, the new direction of active perception can actively decode the tactile information by tuning its sensitivity and specificity with a tunable physical reservoir that filters the signal. In future studies, we will focus on the application of active sensing with the tunable stiffness soft sensors in stiffness discrimination, texture recognition, and designing the soft sensors in more diverse geometries to be integrated with other soft robotic systems.

7. ACKNOWLEDGMENTS

This work was supported by the Engineering and Physical Sciences Research Council (EPSRC) Programme Grant EP/V000748/1 From Sensing to Collaboration: Engineering, Exploring and Exploiting the Building Blocks of Embodied Intelligence and RoboPatient grant EP/T00603X/1.

8. AUTHOR DISCLOSURE STATEMENT

No competing financial interests exist.

9. SUPPLEMENTARY MATERIAL

A. *Materials and sensor fabrication*

B. *FEM*

C. *Sensor characterisation setup*

D. *Stress Relaxation*

Fig. S1:

E. *Manufacturing Repeatability and Effect of Aging*

Fig. S2:

F. *Supplementary Figures with Full Set Data*

Fig. S3: Full data set of Fig. 5

Fig. S4: Full data set of Fig. 6

Fig. S5: Full data set of Fig. 7

Fig. S6: Full data set of Fig. 8

Table S1 Tunable sensing characteristics from experimental characterisation

10. REFERENCES

1. Dahiya, R. S., Metta, G., Valle, M., et al. Tactile sensing—from humans to humanoids. IEEE transactions on robotics 2009; 26(1), 1-20.
2. Lee, M. H., & Nicholls, H. R. Review Article Tactile sensing for mechatronics—a state of the art survey. Mechatronics 1999; 9(1), 1-31.
3. Maiolino, P., Maggiali, M., Cannata, et al. A flexible and robust large scale capacitive tactile system for robots. IEEE Sensors Journal 2013; 13(10), 3910-3917.
4. Seminara, L., Pinna, L., Valle, M., et al. Piezoelectric polymer transducer arrays for flexible tactile sensors. IEEE Sensors Journal 2013; 13(10), 4022-4029.
5. Stassi, S., Cauda, V., Canavese, G., et al. Flexible tactile sensing based on piezoresistive composites: A review. Sensors 2014; 14(3), 5296-5332.
6. Zhao, H., O'Brien, K., Li, S., et al. Optoelectronically innervated soft prosthetic hand via stretchable optical waveguides. Science robotics 2016; 1(1), eaai7529.
7. Wang, H., Totaro, M., & Beccai, L. Toward perceptive soft robots: Progress and challenges. Advanced Science 2018; 5(9), 1800541.
8. Schmitz, A., Maiolino, P., Maggiali, M., et al. Methods and technologies for the implementation of large-scale robot tactile sensors. IEEE Transactions on Robotics 2011; 27(3), 389-400.
9. Alspach, A., Hashimoto, K., Kuppuswamy, N., et al. Soft-bubble: A highly compliant dense geometry tactile sensor for robot manipulation. In 2019 2nd IEEE International Conference on Soft Robotics (RoboSoft 2019) (pp. 597-604). IEEE.
10. He, L., Lu, Q., Abad, S. A., et al. Soft fingertips with tactile sensing and active deformation for robust grasping of delicate objects. IEEE Robotics and Automation Letters 2020; 5(2), 2714-2721.
11. Scimeca, L., Hughes, J., Maiolino, P., et al. Action Augmentation of Tactile Perception for Soft-Body Palpation. Soft Robotics 2021; https://doi.org/10.17863/CAM.64360
12. Sornkarn, N., & Nanayakkara, T. Can a soft robotic probe use stiffness control like a human finger to improve efficacy of haptic perception?. IEEE transactions on haptics 2016, 10(2), 183-195.
13. Sornkarn, N., Dasgupta, P., & Nanayakkara, T. Morphological computation of haptic perception of a controllable stiffness probe. PloS one 2016; 11(6), e0156982.
14. Wegiriya, H., Herzig, N., Abad, S. A., et al. A Stiffness Controllable Multimodal Whisker Sensor Follicle for Texture Comparison. IEEE Sensors Journal 2019; 20(5), 2320-2328.
15. Herzig, N., He, L., Maiolino, P., et al. Conditioned haptic perception for 3D localization of nodules in soft tissue palpation with a variable stiffness probe. PloS one 2020; 15(8), e0237379.
16. Thuruthel, T. G., Hughes, J., Georgopoulou, A., et al. Using Redundant and Disjoint Time-Variant Soft Robotic Sensors for Accurate Static State Estimation. IEEE Robotics and Automation Letters 2021; 6(2), 2099-2105.

17. Scimeca, L., Maiolino, P., & Iida, F. Efficient Bayesian exploration for soft morphology-action co-optimization. In 2020 3rd IEEE International Conference on Soft Robotics (RoboSoft 2020) (pp. 639-644). IEEE.
18. Zou, L., Ge, C., Wang, Z. J., et al. Novel tactile sensor technology and smart tactile sensing systems: A review. Sensors 2017; 17(11), 2653.
19. He, L., Herzig, N., de Lusignan, S., et al. An Abdominal Phantom With Tunable Stiffness Nodules and Force Sensing Capability for Palpation Training. IEEE Transactions on Robotics 2020; doi: 10.1109/TRO.2020.3043717.
20. Holzapfel, A. G. Nonlinear solid mechanics II, 2000.
21. Mullins, L. Softening of rubber by deformation. Rubber chemistry and technology 1969; 42(1), 339-362.
22. Ogden, R. W. Large deformation isotropic elasticity–on the correlation of theory and experiment for incompressible rubberlike solids. Proceedings of the Royal Society of London. A. Mathematical and Physical Sciences 1972; 326(1567), 565-584.
23. Slesarenko, V., & Rudykh, S. Towards mechanical characterization of soft digital materials for multimaterial 3D-printing. International Journal of Engineering Science 2018; 123, 62-72.
24. Liu, L., & Li, Y. Failure mechanism transition of 3D-printed biomimetic sutures. Engineering Fracture Mechanics 2018; 199, 372-379.
25. Abayazid, F. F., & Ghajari, M. Material characterisation of additively manufactured elastomers at different strain rates and build orientations. Additive Manufacturing 2020; 33, 101160.
26. Beebe, D.J., Hsieh, A.S., Denton, D.D., et al. A silicon force sensor for robotics and medicine. Sensors and Actuators A: Physical, 1995, 50(1-2), pp.55-65.
27. Shimojo, M., Namiki, A., Ishikawa, M., et al., A tactile sensor sheet using pressure conductive rubber with electrical-wires stitched method. IEEE Sensors journal, 2004, 4(5), pp.589-596.

SUPPLEMENTARY MATERIAL

A. *Materials and sensor fabrication*

With Polyjet 3D printing, the machine deposits small droplets of photopolymers onto the printing platform through inkjet printing heads, then cures the photopolymer with ultraviolet lamps. The technique also allows several materials to be mixed locally using multiple material-jetting nozzles to create composite materials with different mechanical properties. To off-line tune the sensor stiffness, we used a mixture of soft TangoPlus (Tango+) polymer and stiff VeroClear (mechanical properties similar to Acrylonitrile Butadiene Styrene (ABS)) to produce a series of Digital Materials (DM) with various stiffness. Seven graded materials are prepared for the soft sensor with pure Tango+, and six DM combinations printed from the mixture of the two base materials: FLX9940-DM, FLX9950-DM, FLX9960-DM, FLX9970-DM, FLX9985-DM, and FLX9995-DM. In this paper, a short notion of 40-DM, 50-DM, 60-DM, 70-DM, 85-DM, and 95-DM is used for simplification. The name is also related to the equivalent Shore A hardness of the material. Table. 1 shows the measured Shore A hardness of the seven materials before and after one year of printing. The first measurement was taken after the samples were printed less than 72 hours. The second measurement was taken after around one year the sample been fabricated. The data were collected on four identical samples (cylinder with a diameter of 20 mm and thickness of 3 mm) for 20 trials with a commercial Shore A durometer for each type of material. The samples are stored in a lab environment with exposure to frequent fluorescent light and contact to air under room temperature for the one-year aging test. Up to 9.2% of shore hardness changes are observed for the materials due to the effect of aging. It is interesting to note that no significant material shore hardness variation is found for 50-DM, 60-DM, and 70-DM (shown with p-value > 0.05). In addition, soft materials Tango+ and 40-DM exhibit a stiffness increase in contrast to stiffness decrease in stiff materials 85-DM and 95-DM.

The material stress-strain characterization data are obtained through literature[23,24]. The value of the long-term shear modulus for Tango+, 40-DM, 50-DM, 60-DM, and 70-DM are reported in the study of Slesarenko and Rudykh[23], characterising the material response under the infinitely slow loading. The shear modulus of 85-DM and 95-DM are computed with the Young's modulus data found in [24], where $\mu = 0.5\, E\,/(1+\nu)$ is used as a Linear Elastic model. The materials are considered to be nearly incompressible with $\nu = 0.49$ in the calculation. All shear modulus used in this study are reported in Table. 1.

B. FEM

The FEM simulation is performed with a 3D model in COMSOL Multiphysics 5.3a (COMSOL Inc., Sweden) "Solid Mechanics" module with a "Stationary" study. The soft body of the sensor is modelled with the same parameters used in the state 0 theoretical model (R_0, t_0). The indenter is modelled as a rigid plate (ABS plastic) with a diameter of 30 mm. A nearly incompressible neo-Hookean material model is used in the study for the soft sensors. The material stress-strain relations for the simulation are obtained through literature23,24. Specifically, the shear modulus used for the neo-Hookean model is 0.17, 0.27, 0.55, 0.91, 1.64, 4.00, and 5.33 MPa for Tango+, 40-DM, 50-DM, 60-DM, 70-DM, 85-DM, and 95-DM, respectively. The polymerised density of all the materials is modelled as 1.15 g/cm3 with the Poisson's ratio of 0.49. The base of the soft sensor is assigned as a "fixed" constraint, and pressure is applied to the internal surface of the sensor. The FEM simulation is performed in two studies: (1) the sensor is pressurised freely with a defined driving pressure from state 0 to state I, (2) the rigid indenter is used in state II to exert regulated loading with step control. In study 1, the soft sensor is not in contact with the indenter, and the internal volume of the sensor is increasing with the increase of driving pressure. Thus, inflation can be observed. In study 2, the internal pressure is solved based on the result of study 1 and the governing sensor deformation. The indenter moves step by step to apply increased loading on the sensor. Boyle's law is considered in the simulation. The contact model between the indenter and the sensor surface is modelled as frictionless. During the indentation, the internal pressure of the sensor is modelled as a function of the sensor internal volume, its initial inflated volume, and the driving pressure in study 1.

C. Sensor characterisation setup

The sensor characterisation experimental tests were conducted with a 3-axis Cartesian robot, composed of an ANT130 XY- stage (Aerotech Inc., accuracy of 2.5 μm) and an Actuonix linear actuator (L16-100-63-12-P). The robot carries a probe for the indentation, where a 6-axis Force/Torque sensor (SI- 40-2, ATI Industrial Automation, USA, resolution of 0.02 N) was attached. The soft tactile sensors for characterisation were mounted on the tip of the probe during the tests. The robot pushed the flat surface vertically (z-direction) against the tactile sensors, shown in Fig. 4. The sensor is connected to a pressure sensor (±100 kPa, PSE 543-R06, SMC Corporation, Japan), air pump, and pneumatic valves (Z031 C, Sirai, Italy) to control the internal pressure and measure the internal pressure variation. The force data were collected through a National Instruments data acquisition board (PCIe-6320), while the pressure data from the soft tactile sensors and linear actuator position data were acquired with a National Instrument DAQ (USB-6341). All data were recorded at the frequency of 10k Hz through Labview 2018 with a PC. The experiment was performed under an ambient indoor environment with room temperature (18-26°C). For the pressure sensor, the operating temperature range is 0-50°C with the temperature characteristics of ±2% F.S. or less (Based on 25°C), and the characterised operating humidity range is 35 to 85% which covers the condition for the experiment. According to Boyle's law ($p \propto \frac{1}{V}$, where P is the pressure of the gas and V is the volume of the gas), the influence of temperature on the sensor reading is neglected in this study. The effect of huge temperature fluctuation is not considered in the characterisation.

D. Stress Relaxation

The evaluation of the stress relaxation of the sensor was conducted by maintaining a fixed deformation to the sensor for 10 minutes at a constant room temperature (18-26 °C). The tests were performed on the seven samples with different material stiffness and randomly selected driving pressures (one trial of soft state around 0 kPa, one trial of stiff state around 25 kPa).

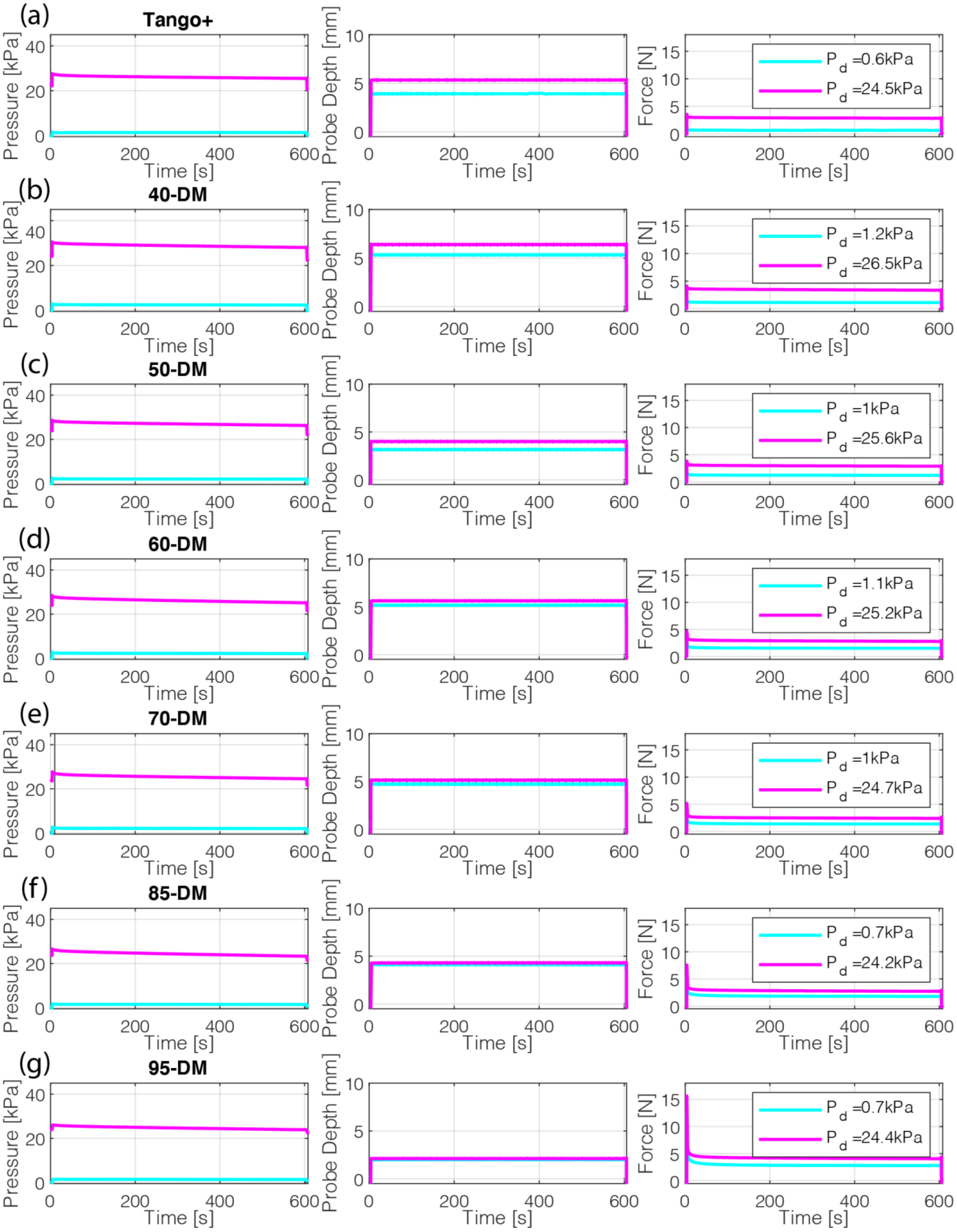

Fig. S1

Fig. S1: The result of the 600 seconds relaxation test for the sensors made from Tango+, 40-DM, 50-DM, 60-DM, 70-DM, 85-DM, and 95-DM at two driving pressures are shown in **(a)** to **(f)**, respectively. The internal pressure, probing depth, and applied force are shown.

Fig. S1 reports the sensor responses, the force sensor response, and the position of the indenter. In general, the response of the sensor and the force sensor shows that stress relaxation is low for this type of sensor. However, the increase of material stiffness would result in increased peak force at the moment of contact. This high-frequency contact force due to collision is difficult to be captured with sensors made from stiffer materials.

E. Manufacturing Repeatability and Effect of Aging

To evaluate the sensor's manufacturing repeatability, the performance variation of the three identical soft sensors with the same material within each group was studied.

To evaluate the effect of the material aging of the sensors, we tested two groups of soft sensors that were manufactured at different times. Samples with the material of Tango+, 50-DM, and 70-DM were used for the tests. Group 1 sensors with three identical sensors of each material that 3D printed around one year before the test. Group 2 sensors with three identical sensors of each material that 3D printed less than 72 hours before the test. The same load-unload pressure cycle was used, as described previously.

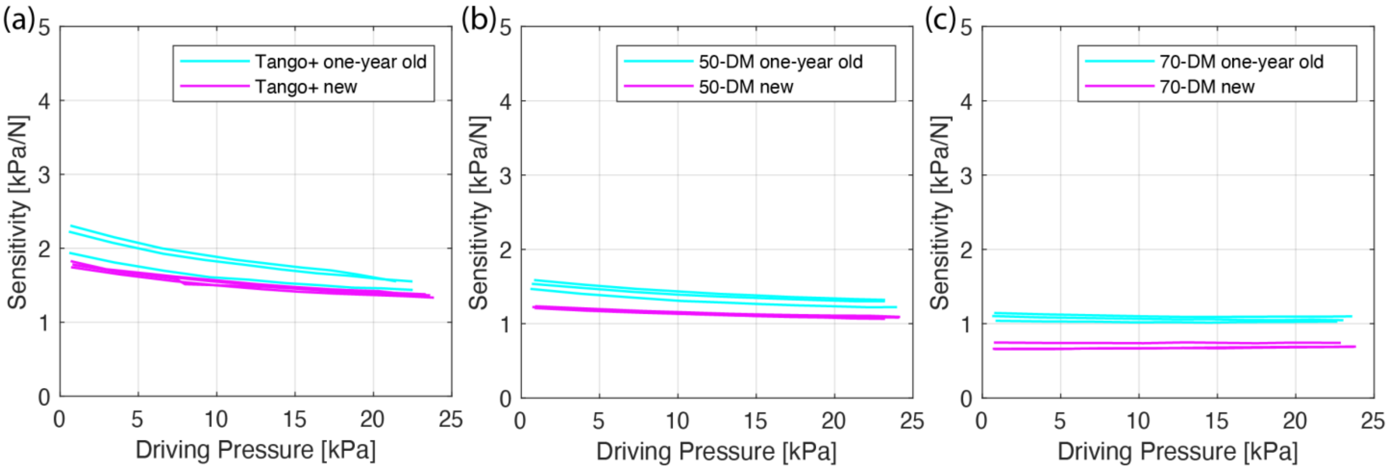

Fig. S2

Fig. S2: Sensitivity results with increased driving pressure from the characterisation are shown for three sensors fabricated one year ago and three sensors fabricated within 72 hours.

Fig. S2 reports the sensitivity of the sensors with the increase of driving pressure. The sensitivity is computed the same as in the previous section.

In general, the sensors show good manufacturing repeatability as the sensitivity curves remain consistent for different sensors. Average standard deviation (with three identical sensors fabricated at the same time) on the sensitivity for sensors made from Tango+ one-year-old, Tango+ new, 50-DM one-year-old, 50-DM new, 70-DM one-year-old, and 70-DM new, are 0.167, 0.035, 0.075, 0.015, 0.054, and 0.051, respectively. Indeed, a difference between the newly fabricated sensor and the sensor fabricated one year ago can be observed due to material aging. The average difference between the sensitivity curve of new sensors and one-year-old sensors for Tango+, 50-DM, and 70-DM are 0.347, 0.305, and 0.489, respectively (equivalent to 14.76%, 16.98%, and 34.9% normalised to the averaged sensitivity curve of the one-year-old sensors).

F. Supplementary Figures with Full Set Data

Fig. S3: Full set results of sensor mechanical property change with both online (driving pressure) and offline (membrane stiffness) parameters. (a) The theoretical modelling result. The colour bar indicates the probing depth of the indentation. The x-axis is the geometry data of the sensor with h_I (state I) at a specific driving pressure. The y-axis is the sensor stiffness characterised by $dF/d\Delta h$. (b) The result from FEM studies. Indentation force with probing depth for sensors with increased driving pressure. (c) The result from experimental characterisation. Indentation force with probing depth for sensors with increased driving pressure. All three-trial data on three identical sensors for each driving pressure are shown in the subplot. Good repeatability of all sensors can be observed.

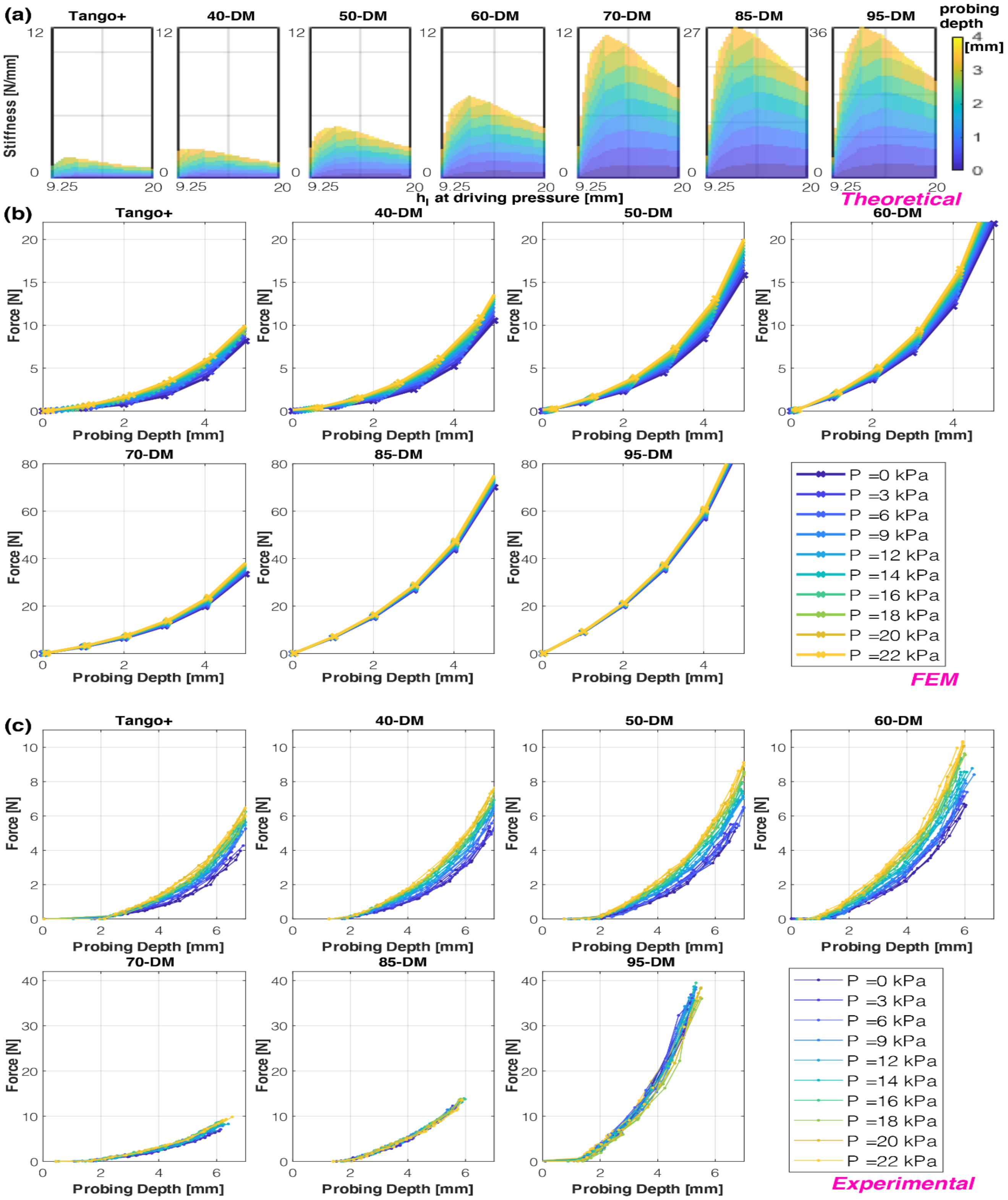

Fig. S3

Fig. S4: Full set sensitivity results from the FEM study. (a) Result of the sensor made from Tango+ under 22 kPa driving pressure, from state 0, I, to II. The deformation, the von Mises stress on the surface, and the contact pressure are shown. (b) and (c) Internal pressure and force data for all sensors made from different materials at the driving pressure of 22 kPa. (d)-(j) The results of sensor response ΔP at different applied forces ΔF is shown in (d) to (j) for different membrane materials, respectively. (k) The overall sensitivity changes of the soft sensors made from different materials with increased driving pressure.

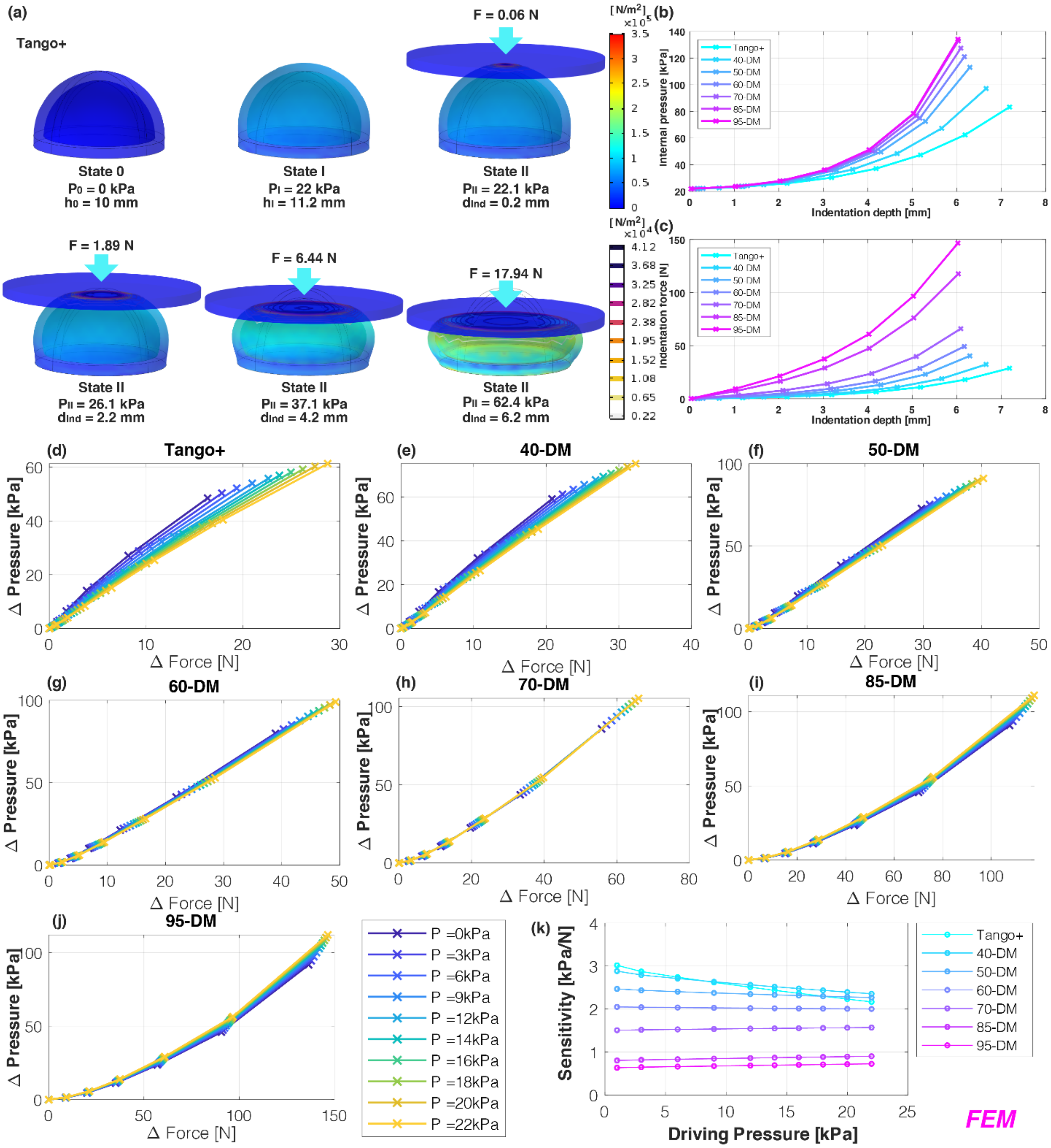

Fig. S4

Fig. S5: Full set results of Fig. 7 (a) Theoretical result of the sensor sensitivity change with increased driving pressure. A zoom view of the experimental tested low-pressure (<22 kPa) region is shown. Part of the curve show two sensitivity values due to the existence of material "snap bulking." During inflation, the membrane will continue to increase its volume after the maximum pressure is reached, yet with reduced internal pressure. (b) Linearity of the sensor response with ΔP and ΔF is represented with R squared value at each driving pressure. (c)-(i) Experimental sensor response with the three trials of repetition on identical sensor samples are shown for each material type. A linear model is used to fit the sensor response. (j) The overall sensitivity changes of the soft sensors made from different materials with increased driving pressure. Standard deviation error shown for repeated tests on three identical samples. Average STD for Tango+, and 40-95 DM are 0.0051, 0.0035, 0.0022, 0.0035, 0.0138, 0.0109, 0.0108, respectively. The average STD for all sensors is 0.0071.

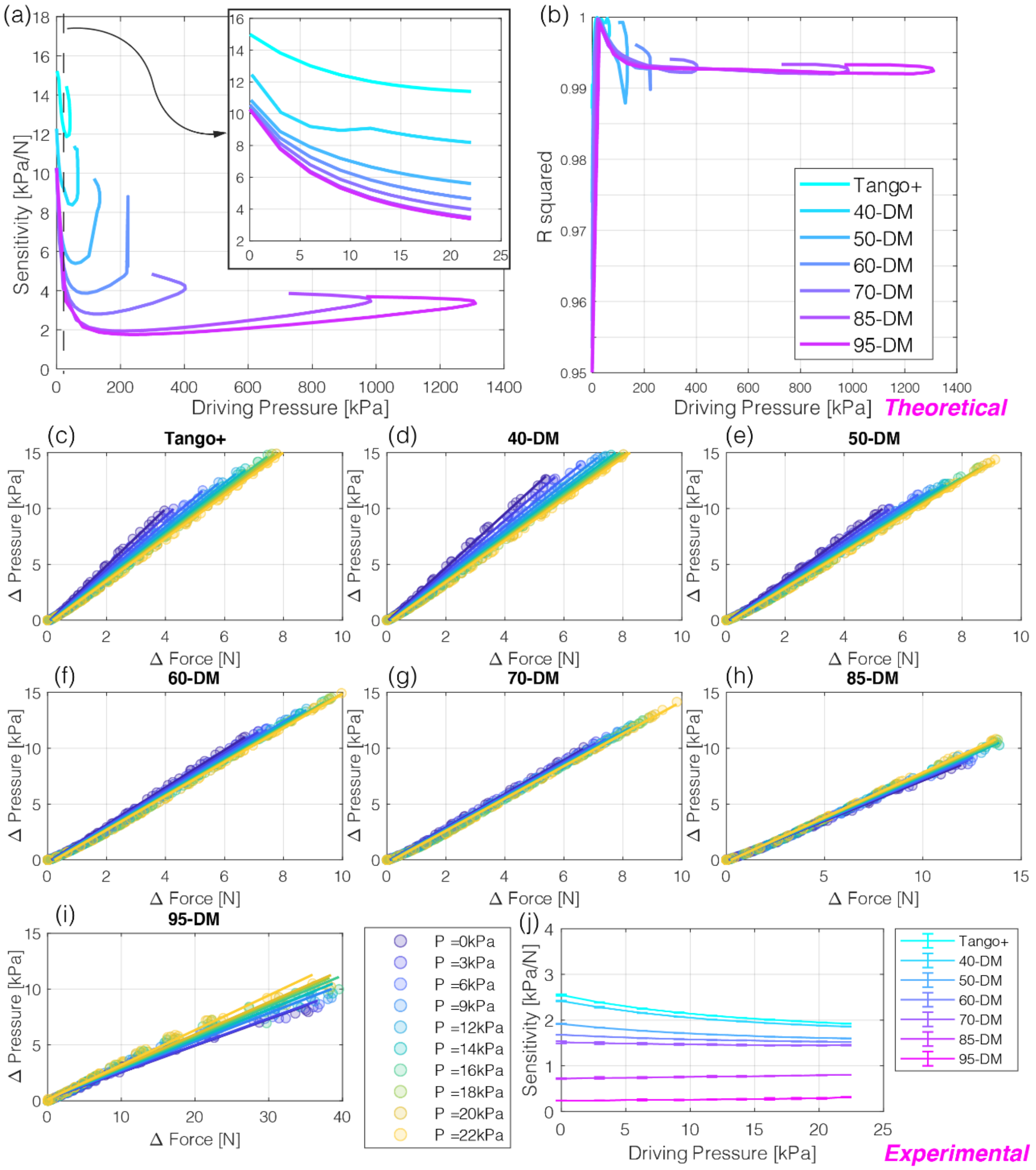

Fig. S5

Fig. S6: Full set result of continuous loading tests. The result of sensors made from Tango+, 40-DM, 50-DM, 60-DM, 70-DM, 85-DM, and 95-DM are shown in (a) to (g), respectively. All sensors are tested in three trials with the driving pressure of 0 kPa and 12 kPa. Sensors made from Tango+, 40-DM, 50-DM, and 60-DM are tested upon saturation. 70-DM, 85-DM, and 95-DM are tested with high loading force. However, the force did not reach saturation, considering the maximum operating force of the cartesian robot. The standard deviation error with the three trials data is shown. (h) Normalised hysteresis.

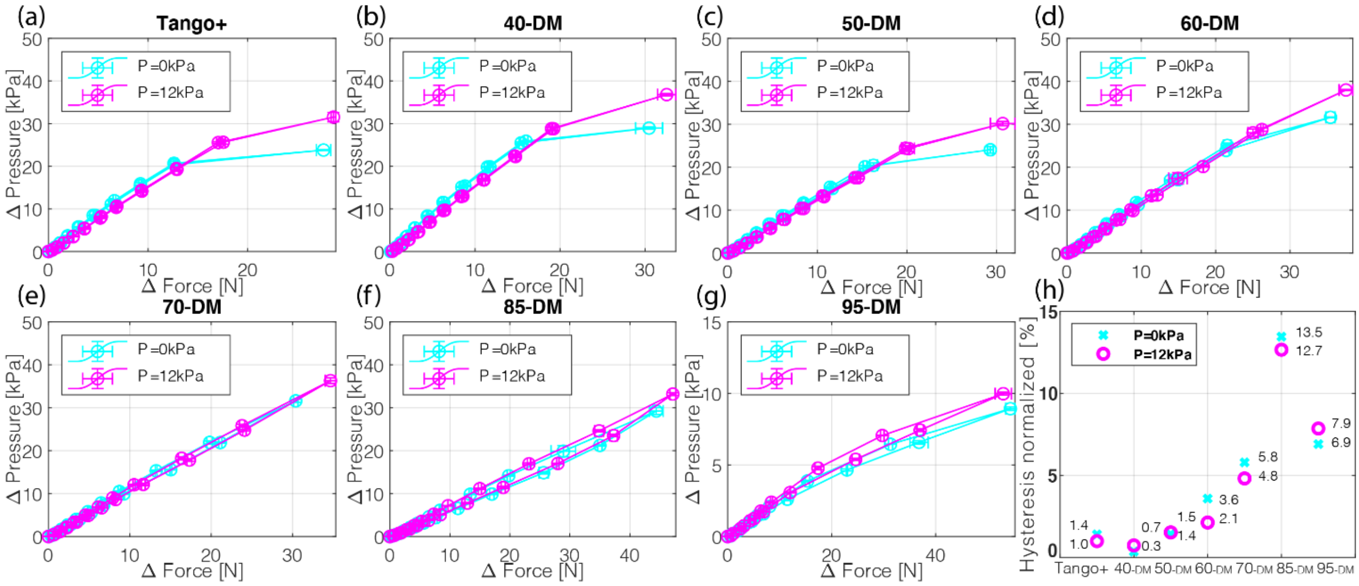

Fig. S6

Table S1 Tunable sensing characteristics from experimental characterisation

Material Type	**Tango +**	**40-DM**	**50-DM**	**60-DM**	**70-DM**	**85-DM**	**95-DM**
Sensitivity at 0 kPa driving pressure [kPa/N]	2.547	2.417	1.915	1.677	1.515	0.720	0.238
Sensitivity at 22 kPa driving pressure [kPa/N]	1.923	1.858	1.598	1.522	1.450	0.803	0.311
Normalised hysteresis at 0 kPa driving pressure (%)	1.4	0.3	1.4	3.6	5.8	13.5	6.9
Repeatability [kPa/N]	0.0051	0.0035	0.0022	0.0035	0.0138	0.0109	0.0108